ORNL/SPR-2019/1347

Light Water Reactor Sustainability Program

Recent Technological Advances in Welding Irradiated Austenitic Steel with Helium

M3LW-19OR0406015

September 2019

U.S. Department of Energy

Office of Nuclear Energy

ORNL/SPR-2019/1347

Materials Science and Technology Division

RECENT TECHNOLOGICAL ADVANCES IN WELDING IRRADIATED AUSTENITIC STEEL WITH HELIUM

M3LW-19OR0406015

Zhili Feng, Roger Miller, Jian Chen, Maxim Gussev, Xunxiang Hu, Wei Tang
Oak Ridge National Laboratory

Gregory Frederick, Jonathan Tatman, Benjamin Sutton
Electric Power Research Institute

September 2019

Prepared by

OAK RIDGE NATIONAL LABORATORY
Oak Ridge, TN 37831-6283
managed by
UT-BATTELLE, LLC
for the
US DEPARTMENT OF ENERGY
Office of Nuclear Energy

under contract DE-AC05-00OR22725

CONTENTS

LIST OF FIGURES

LIST OF TABLES

ACRONYMS

ABSI-LW	Auxiliary beam stress improved laser welding
appm	Atom parts per million
DOE	Department of Energy
EPRI	Electric Power Research Institute
FSW	Friction stir welding
HAZ	Heat affected zone
HeIC	Helium induced cracking
LAMDA	Low Activation Materials Development and Analysis
LTO	Long-term operation
LWRSP	Light water reactor sustainability program
NE	Office of Nuclear Energy
ORNL	Oak Ridge National Laboratory
PWR	Pressurized water reactor
THDS	Thermal helium desorption spectroscopy
VAR	Vacuum arc melting
wppm	Weight parts per million

ACKNOWLEDGMENT

This research was sponsored by the US Department of Energy (DOE), Office of Nuclear Energy (NE), under contract No. DE-AC05-00OR22725 with Oak Ridge National Laboratory (ORNL), managed and operated by UT-Battelle, LLC. Programmatic direction was provided by the Office of Nuclear Reactor Deployment of the Office of Nuclear Energy (DOE NE).

The authors gratefully acknowledge the program support of Thomas M. Rosseel, Materials Research Pathway Lead of the Light Water Reactor Sustainability Program at ORNL, engineering support of Kurt Smith and Bob Sitterson, hot cell facilities and operations contributions of Mark Delph, Clay Morris, Tony Davis, Rick Bowman, Scott Thurman, Scott White, and Allen Smith, characterization and testing efforts of Joshua Schmidlin, Travis Dixon, Stephanie Curlin, and Brian Eckhart, and joining support of Doug Kyle. The authors also wish to thank ORNL staff members Yanli Wang and Lianshan Lin for reviewing this report.

ABSTRACT

This report describes the post-weld study of weld quality and weld properties of irradiated 304 stainless steel made using both Auxiliary Beam Stress Improved Laser Welding (ABSI-LW) and Friction Stir Welding (FSW) processes and conducted in FY 2019. The results demonstrate that both ABSI-LW and FSW processes, developed in this program, mitigated helium-induced cracking during weld repair of helium-containing irradiated SS304 stainless steels. The ABSI-LW method successfully welded SS 304 stainless steel with 15.6 appm He, which is much higher than that has been reported and used by industry. The FSW method successfully welded two different levels of helium (3.4 and 5.2 appm). The findings from this study also suggest pathways to further refine and optimize the two innovative welding processes and possibly the successful welding repair of nuclear reactor internals having helium levels much higher than current weld repair technologies.

This report fulfills the FY2019 milestone M3LW-19OR0406015 “Complete Report on Evaluation of Weld Quality and Weld Properties on Irradiated Stainless Steel Alloys.”

1. INTRODUCTION

Today, welding is widely used for repair, maintenance and upgrade of nuclear reactor components. As a critical technology to extend the service life of nuclear power plants beyond 60 years, weld technology must be further developed to meet new challenges associated with the aging of the plants, such as control and mitigation of the detrimental effects of weld residual stresses and repair of highly irradiated materials. To meet this goal, fundamental understanding of the "welding" effect is necessary for development of new and improved welding technologies.

Welding repair of irradiated nuclear reactor materials (such as austenitic stainless steels used for the reactor internals) is very challenging because the existence of helium in the steel, even at very low levels (i.e. parts per million), would cause cracking during repair welding. Helium is a product of the boron and nickel transmutation process under intense neutron irradiation. Under the influence of high temperatures and high tensile stresses during welding, rapid formation and growth of helium bubbles can occur at grain boundaries, resulting in intergranular cracking in the heat-affected zone (HAZ) – the so-called helium induced cracking (HeIC). Over the past decades, a basic understanding has been established for the detrimental effects of weld stresses on HeIC. However, practical methods for weld repair of irradiated materials are still evolving. Industry's experience has been that, today's arc welding and laser welding based repair technologies are limited for situations where the helium in the irradiated materials is less than 10 appm. It is considered that reactor internals with helium level above 10appm is not weldable (or weld repairable) with current welding processes.

As the service life of nuclear reactors in the US prolongs, the amount of helium in the structural materials in certain highly irradiated areas will continue to increase, reaching levels much higher than 10 appm, as shown in Figure 1 [1]. Therefore, innovations in repair welding technology are essential to address this critical industry need.

This research is a joint DOE/LWRSP and EPRI/LTO effort aimed at developing advanced welding technology for reactor repair and upgrade. It focuses on welding repair of irradiated materials that are extremely challenging and requires long-term R&D. It includes (i) innovations in welding technology for highly irradiated materials, (ii) robust and reliable computational simulation tools to guide process development and predictive application for weld repair of reactor internals, (iii) development of a dedicated welding hot cell capable to perform welding testing on irradiated materials to support welding technology innovations. Two innovative welding processes are under development in this program – auxiliary beam stress improved laser welding/cladding (ABSI-LW), and solid-state friction stir welding/cladding (FSW).

The technology development is also expected to have broad benefit. For example, the proactive stress management and friction stir welding technology may improve the resistance to stress corrosion cracking. The advanced welding simulation tool would provide more reliable prediction of the weld residual stress for component integrity analysis and risk assessment. The DOE LWRSP portion of the project focuses on the fundamental science aspect of the project, whereas the EPRI/LTO part is on the welding system and process development.

This milestone covers the post-weld study of weld quality and weld properties on irradiated 304 stainless steel, make by both ABSI-LW and FSW processes, conducted in the performance period FY2019.

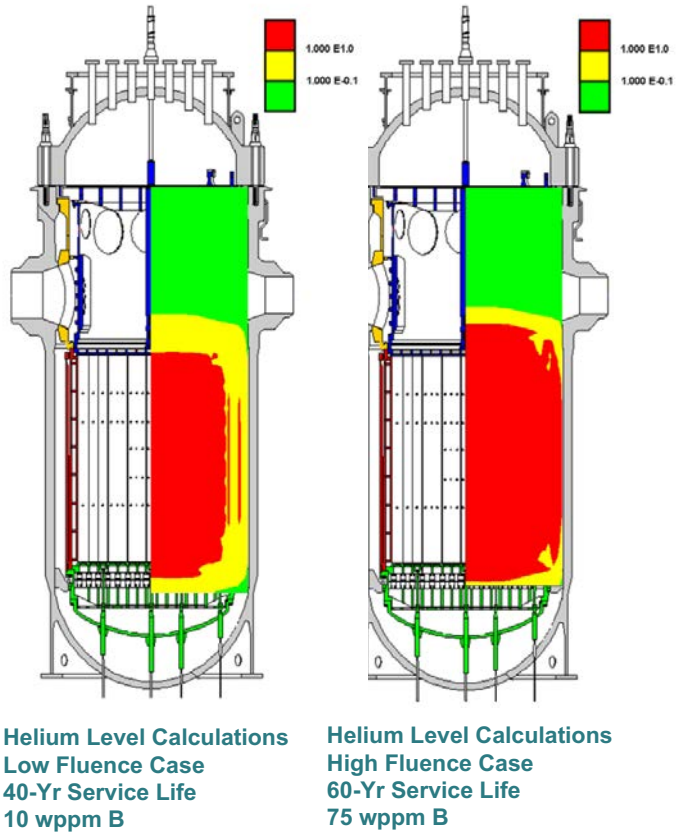

Figure 1 Forecast of helium generation of a typical CE PWR. Red zone: helium generation greater than 10 appm (not weldable with current welding processes). Yellow zone: helium generation greater than 0.1 appm and less than 10 appm (weldable with heat input control). Green zone: helium generation less than 0.1 appm (no special process control is needed). After [1].

2. WELDING

2.1 Materials

Stainless steel SS304 doped with different naturally occurring boron levels were custom made at ORNL. The target B levels were nominally 0, 5, 10, 20 and 30 ppm boron by weight to cover the anticipated helium levels up to 70 years of operation for reactor materials. The custom SS304s were vacuum arc melted (VAR), homogenized at 1050C for 5 hours in air, hot rolled to 19mm thick, followed by cold rolling to 12 mm thick to produce rectangular bar stock. A solution heat treatment (1000C for 30 minutes for SS304 and 1050C for 30 minutes for SS316 followed by water quenching) was then applied to produce acceptable microstructure. Metallographic characterization confirmed that both alloys had satisfactory grain size (less than 100 micron), absence of grain boundary carbides, and acceptable ferrite and martensite levels. The bar stocks were machined to final dimensions (76x56x9mm nominal) to yield 6-8 pieces for each boron level for subsequent irradiation.

Table 1 shows the complete chemistry analysis results of the 5 heats of stainless steels SS304 produced in this project. As shown in the table, the target boron concentrations were achieved. Furthermore, Co concentrations in all samples were extremely low, in the range of 60-80 ppm by weight. This was done deliberately through an exhaustive search of low Co master alloys used in the VAR process. The Co concentrations were kept as low as practically possible, in order to minimize the radioactivity level of the specimens to ease the handling and analysis of irradiated materials during the repair welding experiment and post welding analysis and characterization.

Table 1 Chemistry Analysis Results of SS304

		SS304 Heats				
Element	unit	304A	304B	304C	304D	304E
B	ppm	0.8	4.8	10	24	32
Co	ppm	77	79	79	75	76
Al	ppm	5	5	4	10	5
P	ppm	18	19	19	18	18
S	ppm	14	14	14	15	14
Mo	ppm	390	220	180	240	180
Cu		600	590	610	590	600
C	wt.%	0.012	0.007	0.014	0.01	0.012
Mn	wt.%	1.54	1.55	1.5	1.53	1.52
Si	wt.%	0.49	0.5	0.49	0.49	0.48
P	wt.%	<0.001	<0.001	<0.001	<0.001	<0.001
S	wt.%	0.002	0.003	0.002	0.002	0.002
Cr	wt.%	19.53	19.54	19.28	19.33	19.14
Ni	wt.%	10.61	10.52	10.35	10.41	10.25
Mo	wt.%	0.05	0.04	0.04	0.04	0.04
Cu	wt.%	0.05	0.05	0.05	0.05	0.05
N	wt.%	0.035	0.032	0.035	0.035	0.035

The custom SS304 blocks were irradiated at the High Flux Isotope Reactor (HFIR) of ORNL, with a total fluence in the range of $4.5x10^{20}$ to $1.3x10^{21}$. The irradiated SS304 steel blocks were cooled down for over 2 years before welding experiments.

The SS304 heats with 3 different boron levels were analyzed in this milestone reporting period. The coupon ID were 304B-1 (4.8 wppm B), 304C-6 (10 wppm B), and 304D-1 (24 wppm B).

2.2 Welding

Both ABSI-LW and FSW were conducted at the dedicated welding hot cell at the Radiochemical Engineering Development Center (REDC) of ORNL. For this performance period, three welds – one ABSI-LW and two FSW – have been characterized. The weld coupon ID, boron and helium concentration, and welding processes for the three welds are given in Table 2.

Table 2 Weld coupon ID

Weld coupon No	Boron, wppm	Helium, appm	Welding Process
304B-1	4.8	3.4±0.4	FSW
304C-6	10	5.2±1.1	FSW
304D-1	24	15.6±3.6	ABSI-LW

The basic welding parameters for FSW is in Table 3. Both friction stir welds (304B-1 and 304C-6) were a single pass bead on plate weld shown in Figure 2. The welding direction was from left to right. There appeared a surface defect at the end of the weld, extending into the irradiated materials.

Table 3 FSW Parameters

Parameter	*Value*	*Units*
Starting Position	4.500 (x), 0.000 (y), 2.747 (z)	inch
Tool Rotation Rate	+400 (counter clockwise)	rev/min
Tool Tilt Angle	0	degrees
Welding Speed	0.033	inch/sec
Weld Path Z Travel	0.342	inch
Plunge Speed	0.004	inch/sec
Weld Length	4.0	inch

Laser weld cladding was done on coupon 304D-1. There was a total of 4 laser cladded pads as illustrated in Figure 3: two on the top side of the steel plate and two on the bottom side. Each layer consisted of 3 multi-pass clad layers. Weld ID 1 and Weld ID 4 in the figure were made with the ABSI-LW, whereas Weld ID 2 and Weld ID 3 were with regular LW for comparison. The basic laser welding parameters are summarized in Table 4. Weld 1 and Weld 2 were considered as **High Speed LW**, and Weld 3 and Weld 4 the **Low Speed LW**. The different welding speed and corresponding wire feed rates resulted in different clad layer height.

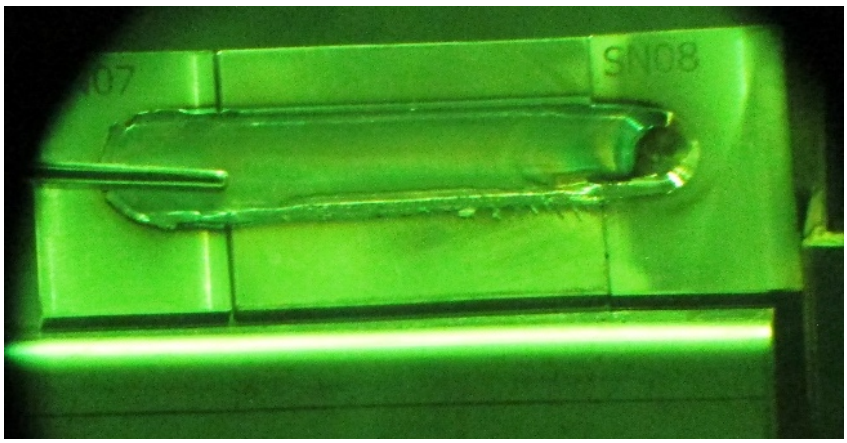

Figure 2 FSW of 304D-1

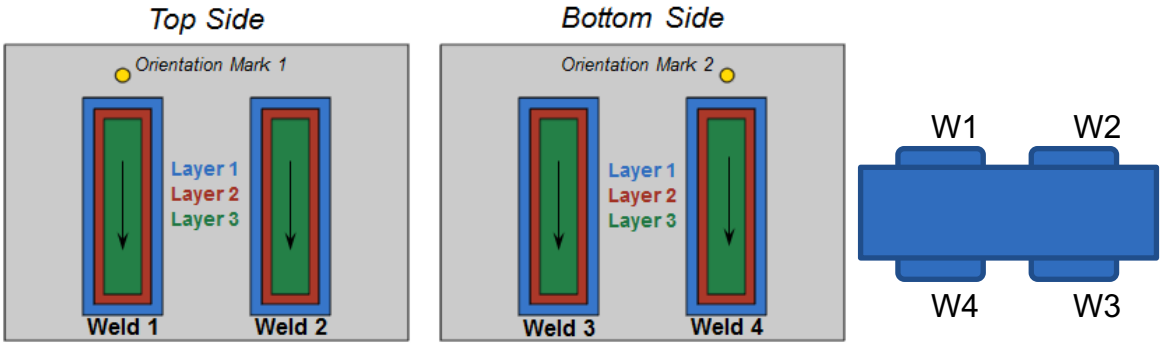

Figure 3 Weld Layout for LW of Irradiated Coupons; Arrows Indicate the Welding Direction.

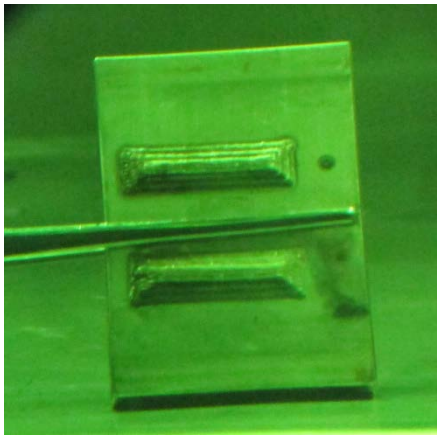

Figure 4. Completed Laser Welds 1 and 2 on Irradiated Coupon 304D-1; Welds 3 and 4 were Completed on the Other Side of the Coupon (Not Visible).

Table 4 Laser welding parameters

	Weld 1	**Weld 2**	**Weld 3**	**Weld 4**
Travel speed (inch/s)	0.45	0.45	0.083	0.083
Wire feed speed (inch/s)	60	60	15*	17**
Welding laser power (w)	1000	1000	1000	1000
Welding laser diameter (mm)	2	2	2	2
ABSI	No	Yes	No	Yes
ABSI laser power (W)	N/A	2000	N/A	368
ABSI laser diameter (mm)	N/A	7.5	N/A	7.5
Heat input from welding beam (J/inch)	2222.2	2222.2	12048.2	12048.2
Heat input from raster beam (J/inch)	0	4444.4	0	4433.7

** Increased to 17 in/s on layer 1, pass 5 and after*

*** Increased to 17 on Layer1-Pass 4 and after*

3. HELIUM MEASUREMENT

Three heats (304B, 304C and 304D) of B-doped and neutron irradiated SS304 steel were analyzed for their helium concentration at ORNL's LAMDA laboratory. Samples from the base metal of the SS304 steel were cut into small pieces (around 2x3x3mm) to fit the tungsten sample holder for thermal helium desorption spectroscopy (THDS) experiment. Two 304B, two 304C and three 304D samples were prepared for the helium measurement. Boron concentration and mass of all samples are listed in Table 1.

Table 5 Sample mass and boron concentration for helium measurements

	Boron Concentration (wppm, nominal)	Mass (g)		
		Sample 1	Sample 2	Sample 3
304B	4.8	0.2199	0.2039	
304C	10	0.3272	0.2369	
304D	24	0.1491	0.1309	0.1288

The THDS measurement heats a sample above its melting temperature in high vacuum, thereby bonding it to the sample holder in the measurement. Thus, a tungsten sample holder was used for each measurement. The sample holder opening was covered by a perforated tungsten cap to ensure the molten material contained within the crucible. Before THDS experiments, the tungsten sample holder was baked in a high vacuum furnace at 1600˚C for 24hrs to remove surface contaminations.

Desorbed helium from the sample was measured by a Pfeiffer quadrupole mass spectrometer. Calibration of the mass spectrometer was performed by using a Vacuum Technology Incorporated (VTI) standard helium leak. Two sets of calibration were performed to ensure good repeatability. Helium background of the THDS system with an empty sample holder was measured from room temperature up to 1450˚C using a linear ramping rate of 0.5˚C/s. Finally, the THDS of all eight 304 steel samples were measured following the identical temperature profile as background measurement. For each THDS measurement, temperature was held at 1450˚C until helium signal comes down to the steady state (i.e. no more desorbed helium from sample).

Figure 5 shows the mass spectrometer calibration result with a VTI standard helium leak. Two calibrations were performed. The transient at the beginning of each calibration was caused by the gas flow instability at the moment when the valve connecting standard leak and the system opens. The steady state flow following the transient was the gas flow data for calibrating electrical current to helium gas flux. The average of steady state current is 1.70×10^{-12}C/s (averaged from 200 – 300s) for the first calibration and 1.69×10^{-12} C/s (averaged from 500 – 600s) for the second calibration, indicating good calibration repeatability. The conversion factor between the electrical current to helium flux is thus 0.237 mol/C based on the VTI standard flow rate (4×10^{-13} mol/s). Figure 6 shows the helium background measurement with y-axis unit converted from current to flow rate by the conversion factor. For the subsequent THDS measurement of actual samples, background subtraction was performed to obtain the helium release from the samples only.

Figure 7 to Figure 9 show the THDS results of 304B, 304C and 304D samples, respectively. Note that the unit of y-axis changes to normalized helium flow with respect to mass to compare results from samples of the same boron concentration but different masses. Table 2 listed the helium concentration in each sample by integrating the total desorbed helium from the THDS results. The variation of helium concentration for samples of the same boron concentration can be understood from their THDS in these figures. For samples with the same boron concentration, the shape of the curves for 304B (4.8 wppm B) and 304C (10 wappm B) before 1450˚C is basically the same. However, for 304D (24 wppm B), the

desorption peak at ~1400˚C is broader for sample 1 than that of sample 2 and 3. The broader peak may be caused by instability of the pump close to the melting point of SS304 steel which leads to much higher helium concentration in 304D sample 1 than that in 304D sample 2 or sample 3. On the other hand, the amount of helium released during holding at 1450˚C is slightly different between samples of the same boron concentration. This explains the small helium concentration variation between 304B sample 1 and sample 2, 304C sample 1 and sample 2 and 304D sample 2 and sample 3. Overall, the helium concentrations of the three SS304 with different amount of B are summarized in Table 6.

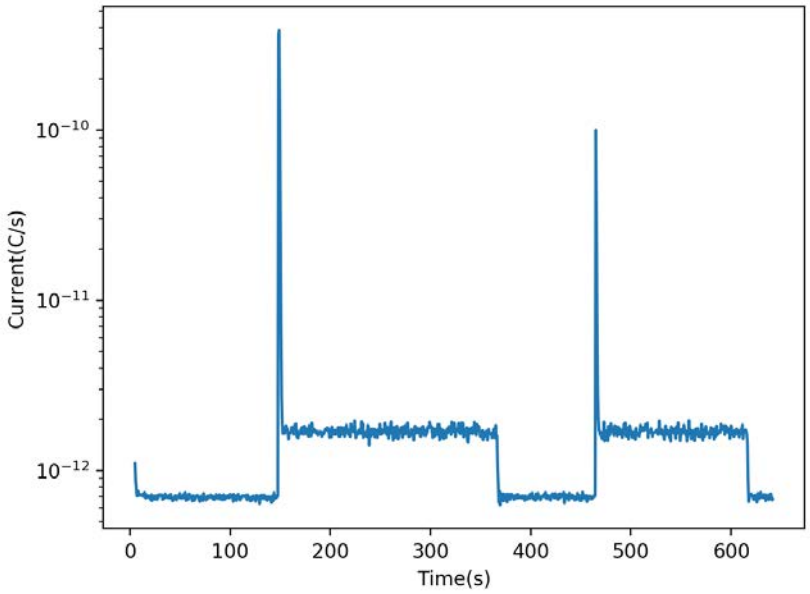

Figure 5 Mass spectrometer calibration for helium signal

Table 6 Helium concentration of 304 steel samples measured from THDS

	Boron Concentration (wppm, nominal)	Helium Concentration (appm)			
		Sample 1	Sample 2	Sample 3	Average
304B	4.8	3.6	3.1		3.4±0.4
304C	10	5.9	4.4		5.2±1.1
304D	24	19.2	12.1	15.5	15.6±3.6

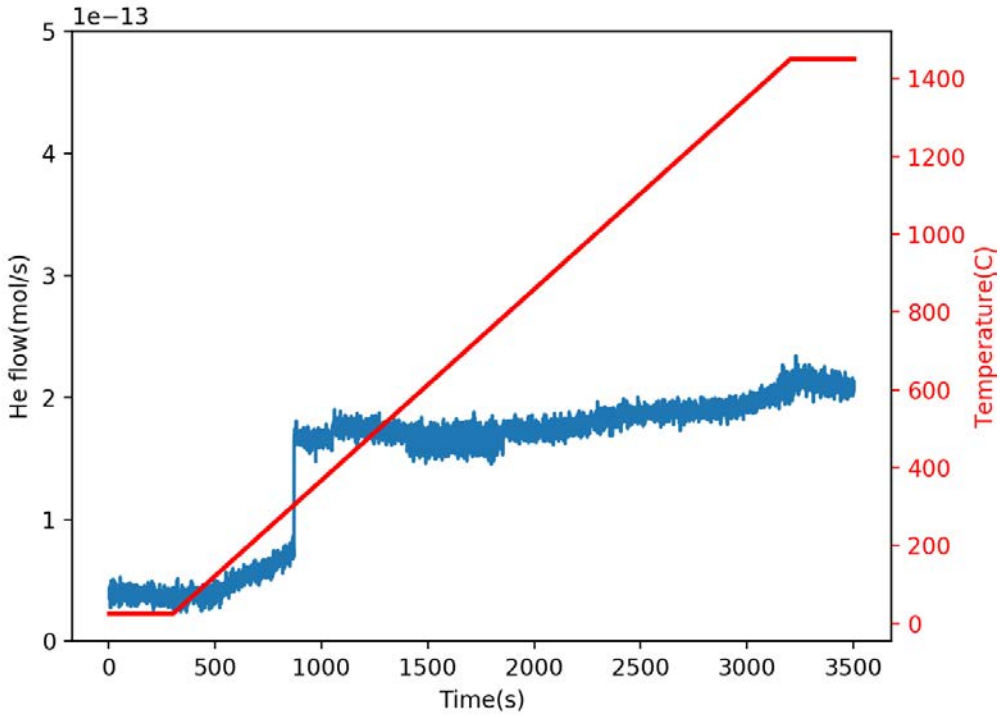

Figure 6 He background measurement up to 1450˚C

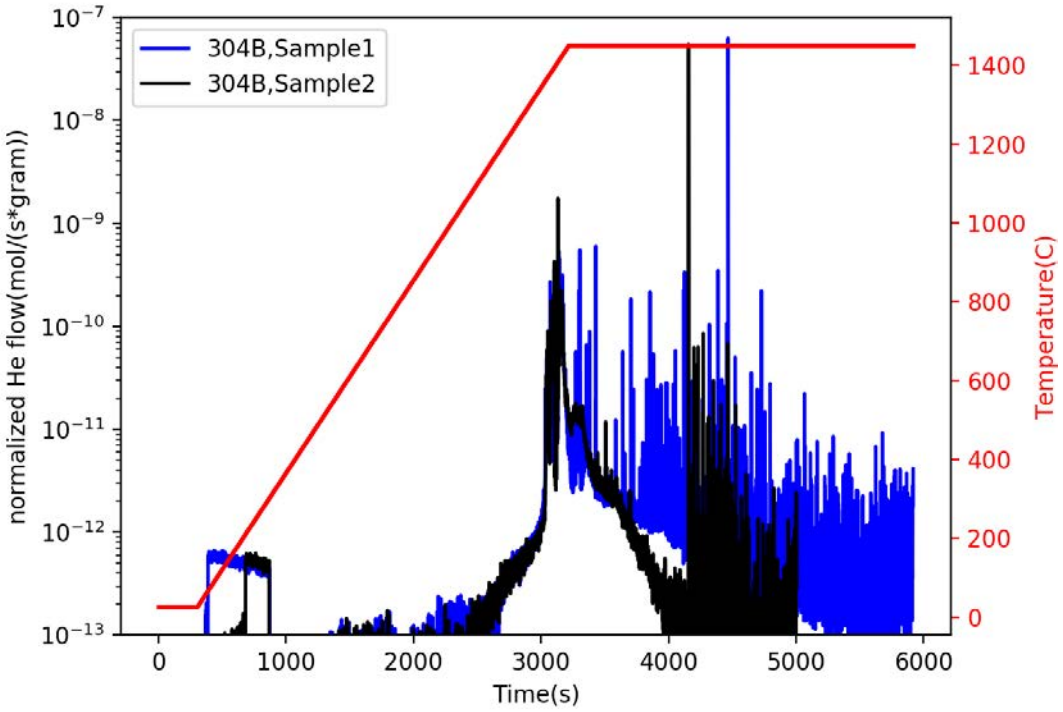

Figure 7 Normalized THDS of 304B samples

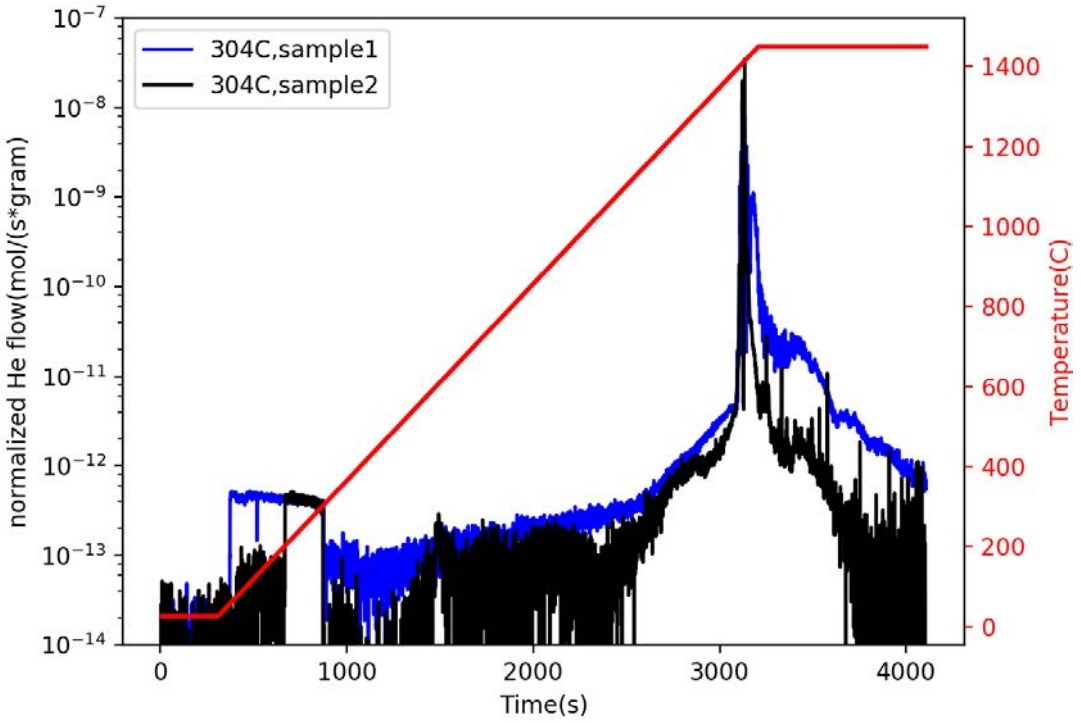

Figure 8 Normalized THDS of 304C samples

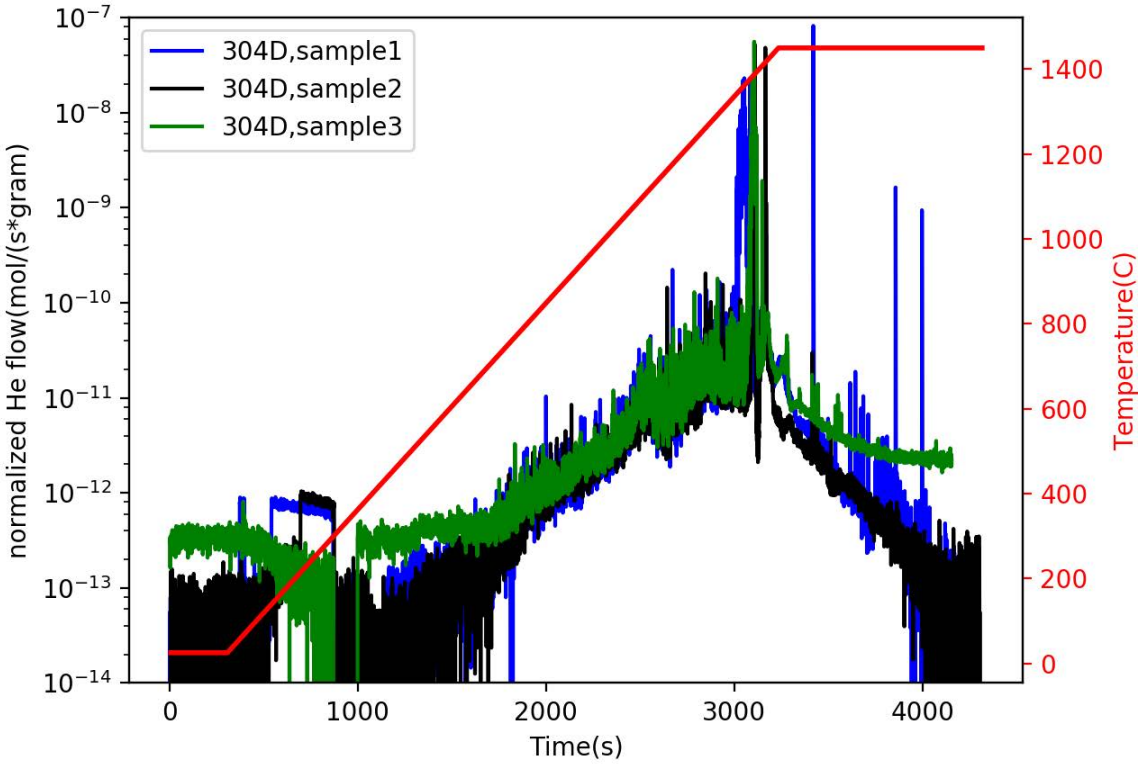

Figure 9 Normalized THDS of 304D samples

By selecting one sample of each boron concentration, Figure 10 compares the helium desorption behavior of samples with different boron concentration before the 1450˚C holding. According to first order dissociation kinetics model, the rate of change of helium content in steel sample can be expressed as:

$$\frac{dN}{dt} = -Nvexp(-\frac{E}{k_B T}) \quad (1)$$

where N is the remaining helium number density in the sample, k_B is the Boltzmann constant (8.617×10^{-5} eV/K), v is the Debye frequency (10^{13}/s) and E and T is the activation energy and temperature corresponding to the desorption peak, respectively. Since the heating rate, β, is constant in this experiment (0.5K/s), we denote $\frac{dN}{dt} = \beta$. The above differential equation can then be solved under the condition $\frac{d^2N}{dt^2} = 0$

$$\ln\left(\frac{\beta}{T^2}\right) = -\frac{E}{k_B T} + \ln\left(\frac{vk_B}{E}\right) \quad (2)$$

On the upper x-axis, we utilize the above solution to compute the activation energy to correlate helium desorption events (represented by the desorption peaks in the spectra) with mechanism at atomic scale. Two quick observations can be drawn from this figure: first, a distinct desorption peak shows up at ~1400˚C for all three samples, corresponding to melting of the steel samples. Second, although desorbed helium signal starts to show up at ~700 ˚C for all three samples, the desorption behavior between 700 and 1400 ˚C are different. Desorbed helium flux steadily increases with a constant slope for 304D (24 wppm B). There also seems to be a broad desorption peak at ~1100˚C. For 304C (10 wppm B) and 304B (4.8 wppm B), helium flux increases slowly from 700 to 1200 ˚C, then increase more rapidly from 1200 to 1400˚C. In general, for all three samples of different boron concentration, almost no helium is dissociated from weak helium traps (i.e. helium-rich vacancy clusters, line dislocations and dislocation loops [2] [3] [4] with low activation energy (<2eV). Some helium is trapped in stable but small helium-vacancy clusters, such as clusters with helium number to vacancy number ratio close to 1:1 [5] [6]. These types of traps have activation energies range from 2.3 to 3.7eV, corresponding to helium release events take place between 800 to 1200˚C.

Cumulative helium desorption, as shown in Figure 11, reveals some other aspects of helium desorption behavior at different boron concentrations. First, the amount of helium desorbed before 1450˚C annealing is drastically different between 304C/304D and 304B. 80% of helium in the sample desorbed before 1450˚C for 304D and 90% for 304C. However, only ~20% of helium desorbed before 1450˚C for 304B. Second, while the cumulative helium release is composed of one step function for sample 304C, it is composed of two step functions for 304B and 304D. The results suggest while most of the helium (>80%) is desorbed before melting for 10 wppm and 20 wppm boron doped samples, the majority of the helium (>70%) generated during neutron irradiation is still retained in strong helium traps, possibly stable helium bubbles, in the 5 wppm boron doped sample close to melting temperature.

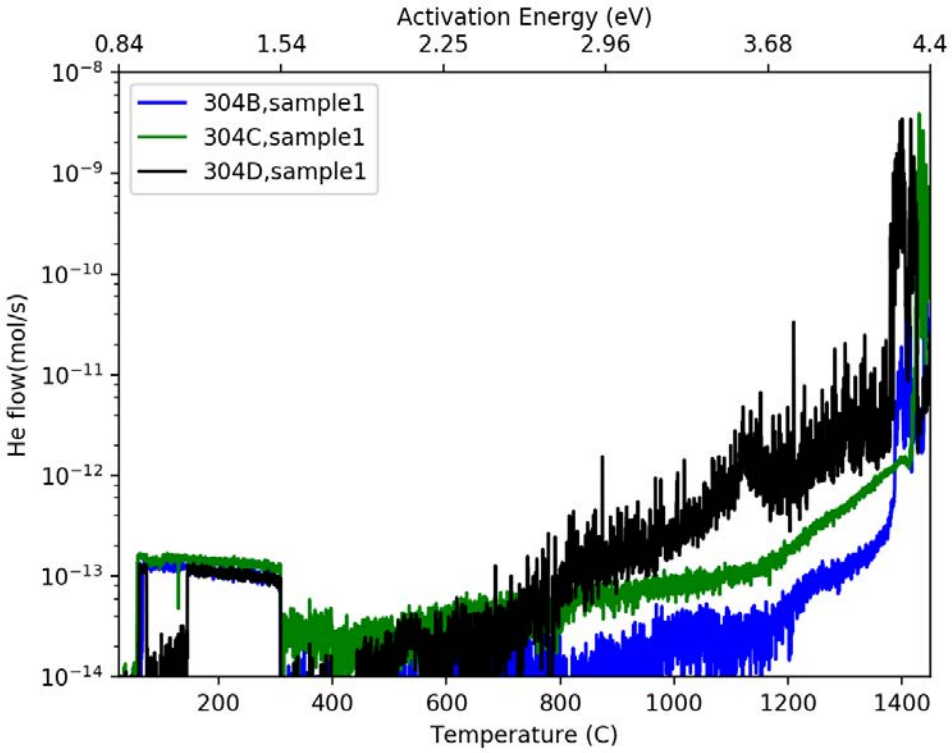

Figure 10 Comparison of THDS behavior before melting between three samples of different boron concentration.

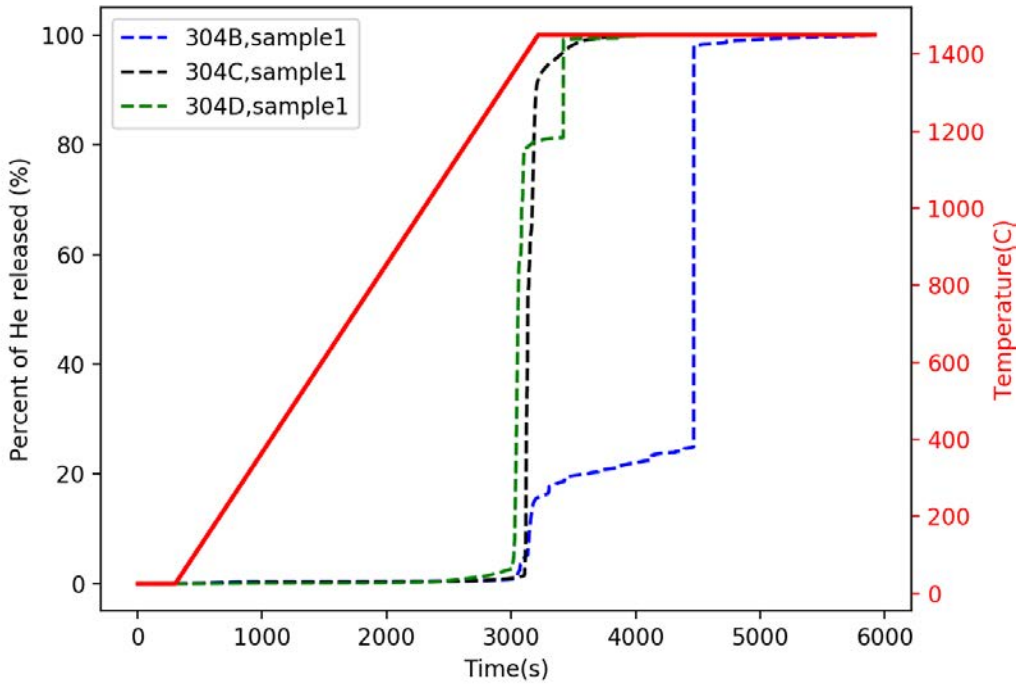

Figure 11 Comparison of cumulative He release between three samples of different boron concentration.

4. WELD QUALITY EVALUATION

Cross-weld metallographic samples were EDM cut from the irradiated weld for both weld quality (i.e. weld defects) and microstructure and property characterization. As shown in Figure 12, 3 cross-sections were cut from each FWS, labeled as 304X-X-6, 304X-X-8, and 304X-X-15, where X-X representing different FSW (304B-1 or 304C-6). It is noted that 304B-1-6 and 304C-6-6 are located near the end of the weld where surface defects were observed in Figure 4. The other sections were taken from the middle of the weld, where no apparent surface defects were observed. Figure 13 shows the location of metallographic samples on the laser welded coupon (304D-1).

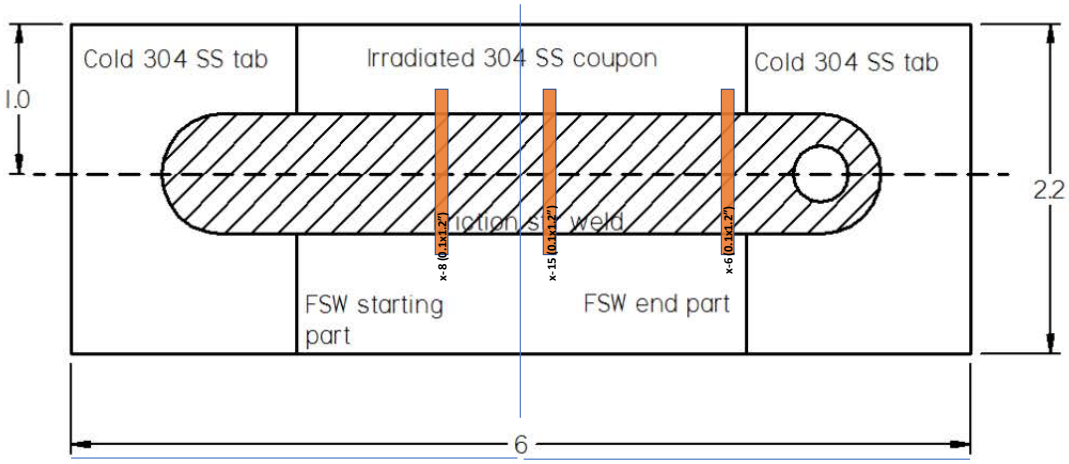

Figure 12 Locations of metallographic samples from the FSW

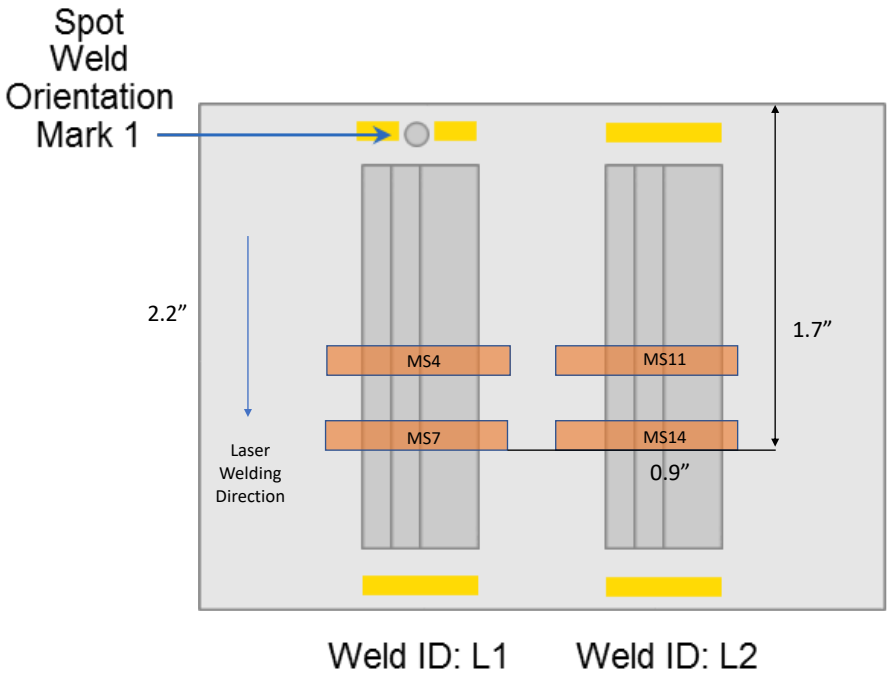

Figure 13 Locations of metallographic samples from the LW

4.1 Friction stir welds

The overall macroscopic cross-section views of the two FSW (304B-1 and 304C-6) are shown in Figure 14. In the middle length of the weld, FSW shows a sound weld without macroscope cracks or weld defect (Figure 14 top view). At the end of weld (middle photo), lack of bonding surface defect showing in the top surface of the weld in Figure 2 extended to a depth of approximately 1-mm. In addition, some spots of voids were apparent at the bottom of the FSW and underneath the weld surface (bottom figure). It is noted that friction stir welds on irradiated SS304 resembles these made on unirradiated SS304 under the same welding conditions. Overall, the results from FSW are very encouraging – millimeter sized cracks in the HAZ of a weld that are characteristic of HeIC are absent in both friction stir welds.

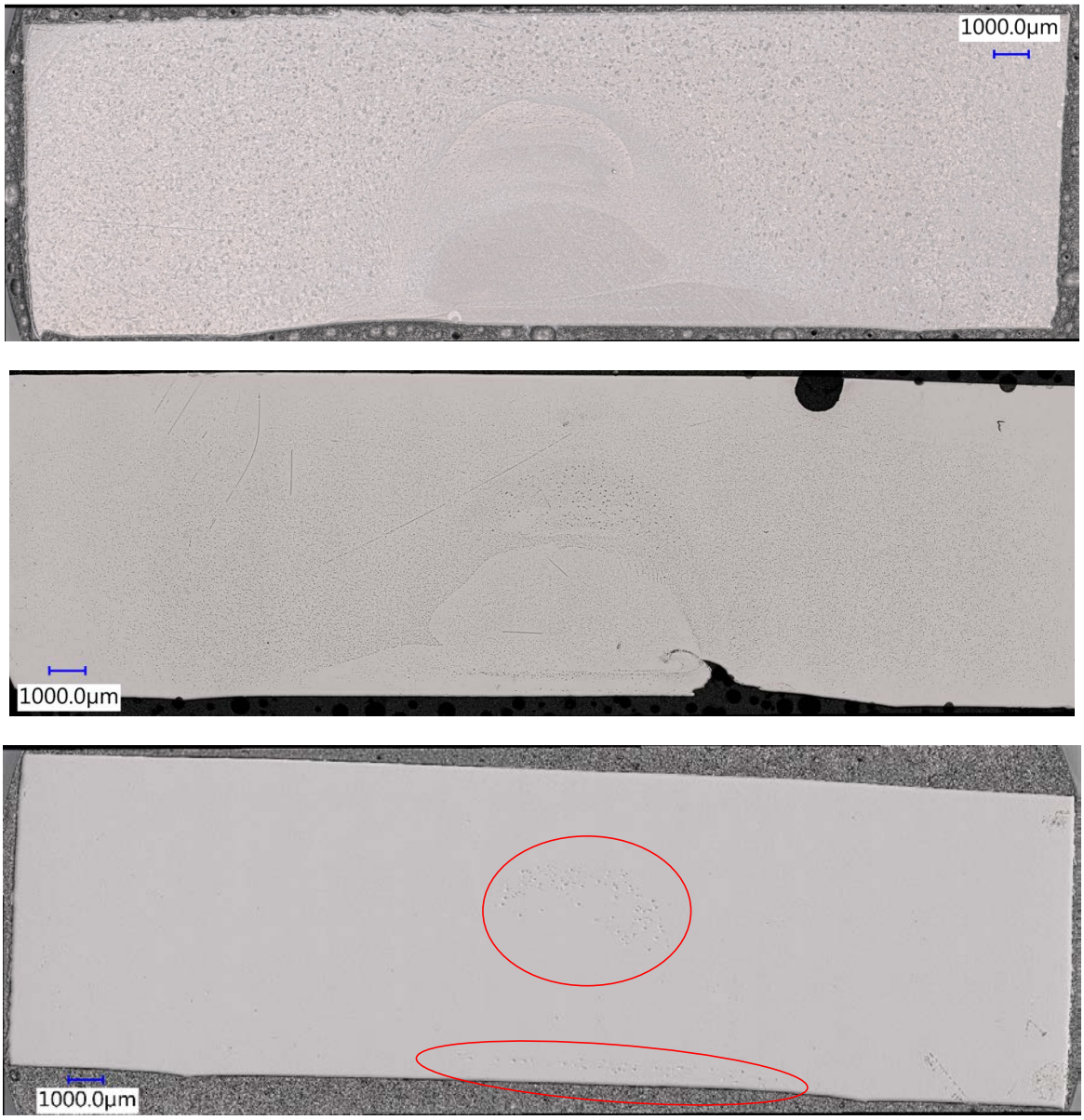

Figure 14 Macro cross-section overview of FSW. Top: etched 304C-6-8. Middle: etched 304B-1-6 near the end of the weld. Bottom: 304B-1-15 Polished only.

Detailed microstructure and microscopic features for 304C-6 FSW with 5.2 appm helium were reported in Milestone Report M2LW-19OR0406014 “Develop Parameters and Characterize the Quality of Friction Stir and Laser Weld-Repaired, Irradiated Structural Materials Representative of Extended Reactor Service Life” (April, 2019). The spots shown in the middle and bottom photo in Figure 14 were microscopic voids less than 2-3 micrometer in size the weld. (Note that these spots were able observed on 304C-6 welds, although it was hard to see in the top photo due to different etching to better distinguish the weld and the base metal). In addition, weld tool debris were also found at the bottom of the stir zone. Tungsten, Rhenium and nitrogen, both are major elements in the polycrystal boron nitride (PCBN) tool were detected. W-enriched layer with W-enriched particles and nitrogen-rich objects are widely presented in the weld zone root region as shown in Figure 15. While SEM/EDS could not reliably detect boron which is the primary element in the tool, the presence of boron would be expected co-existing with other tool alloys elements in the tool debris. The existence of tool debris inside the weld near the weld bottom is consistent with the extensive tool wear especially the tool pin experienced in the FSW trials. This suggests that further FSW process development and optimization is necessary to address the tool wear issue. We note that boron is a major concern after the weld repair, as it would transmute to helium upon neutron irradiation.

Under high magnification SEM, micron sized voids were observed along the ground boundary in the HAZ of the FSW. This is similar to grain boundary deterioration found in other researches. The size of such void/cracks are so small, its influence on the mechanical property and structural integrity of the repaired components is a subject of on-going study.

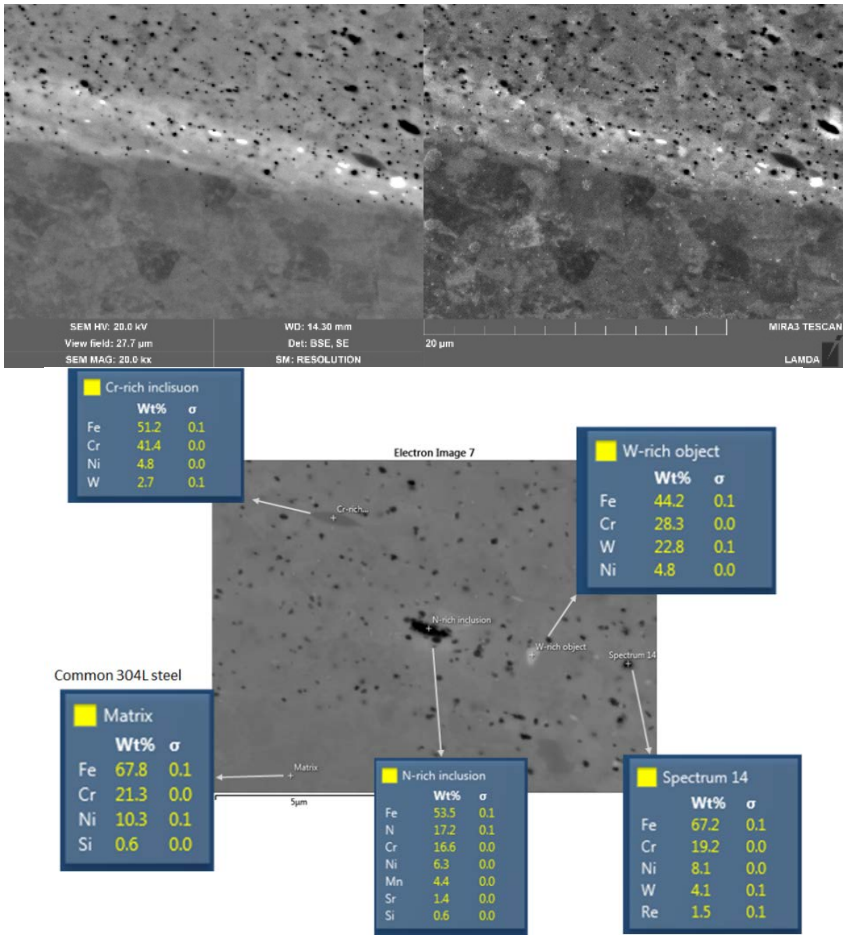

Figure 15 Distribution of weld tool debris and chemistry analysis of the particles representing tool debris.

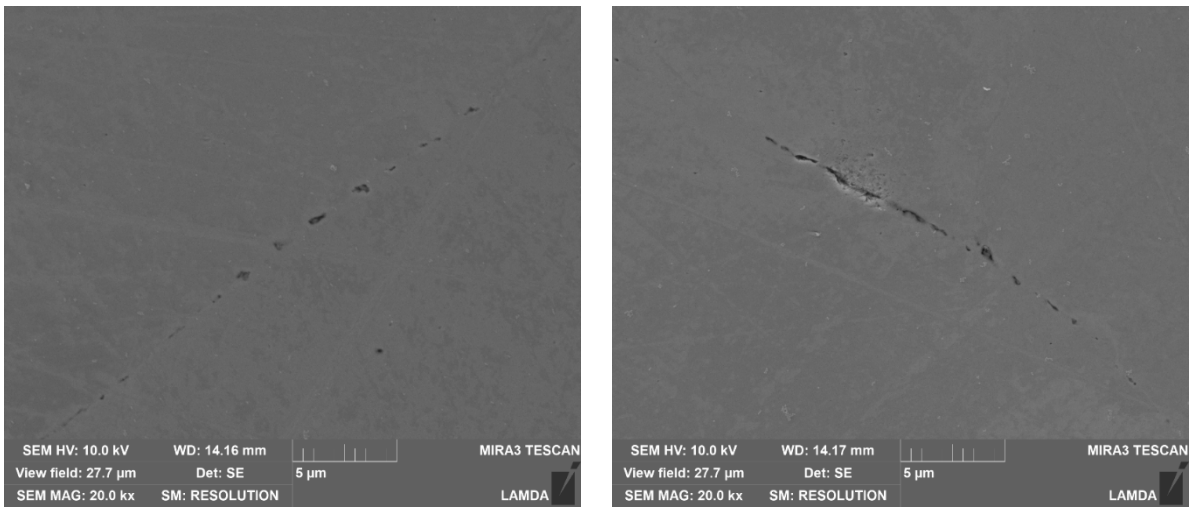

Figure 16 Micro-void like features with about 1 - 2 µm size in a small portion in HAZ

4.2 Laser welds

Figure 17 shows the cross-sectional appearance of the 4 laser weld clads made on 304D-1 under lightly etched surface. The welding conditions for the 4 clads are in Table 4. It is noted that 304D-1 contains 1.56 appm He based on THDS analysis in Section 3. At such a high He level, HeIC would be expected using today's weld repair technology. On the other hand, as shown in Figure 17, there were no apparent mm sized cracks produced in this work.

Sub-millimeter sized porosities or voids were observed inside the fusion boundary of the weld under high welding speed conditions, as shown in Figure 17 (a) and (b). Such porosities were much reduced when welded at lower welding speed. This suggested the direction to refine the laser welding techniques to eliminate these fusion boundary porosities.

Figure 18 shows the same four laser weld clads with heaving etching to reveal the weld region. Again, macro-level cracks were absent in the laser weld clad.

Microcracks in the range of 20 to 50 microns were observed under high magnification SEM (Figure 19). Preliminary comparison suggested that laser weld made with ABSI exhibits much less micro cracks compared to the weld without ABSI under otherwise same welding conditions.

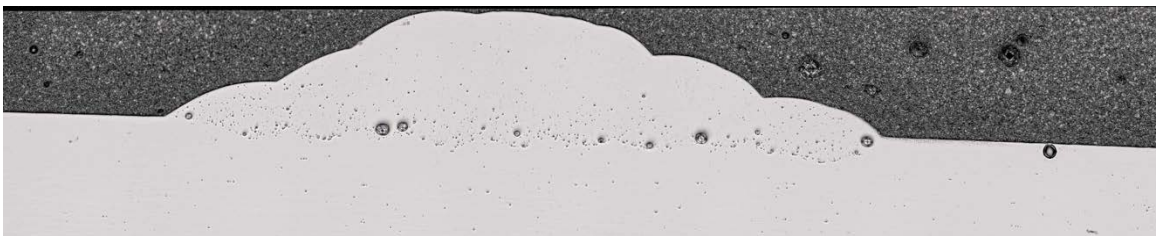

(a) 304D-1-MS4 high speed, w/o ABSI

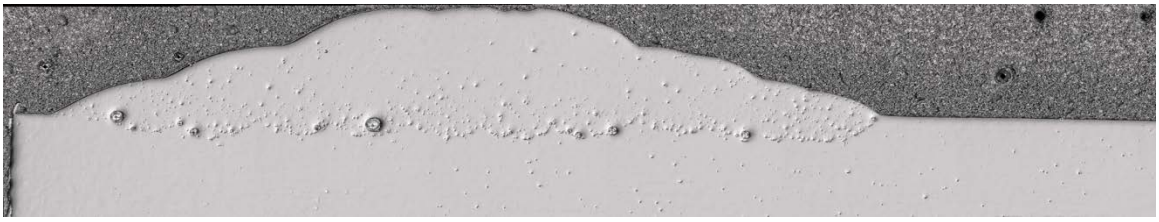

(b) 304D-1-MS11 high speed, ABSI

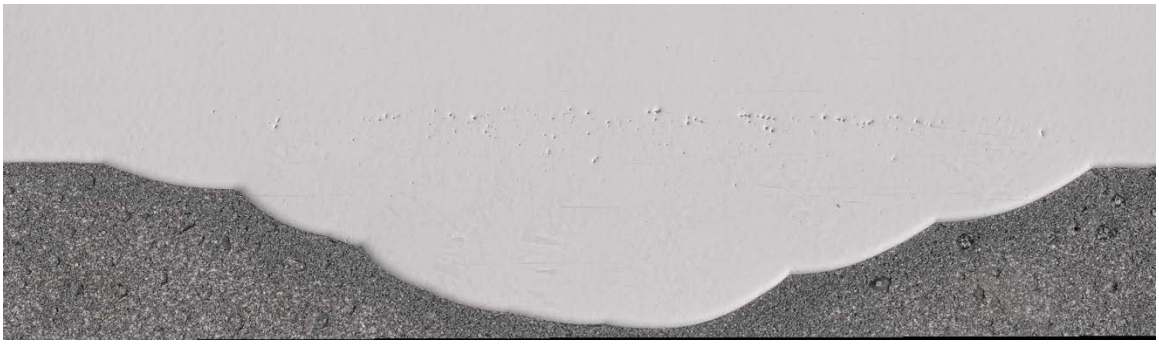

(c) 304D-1-MS11 low speed, w/o ABSI

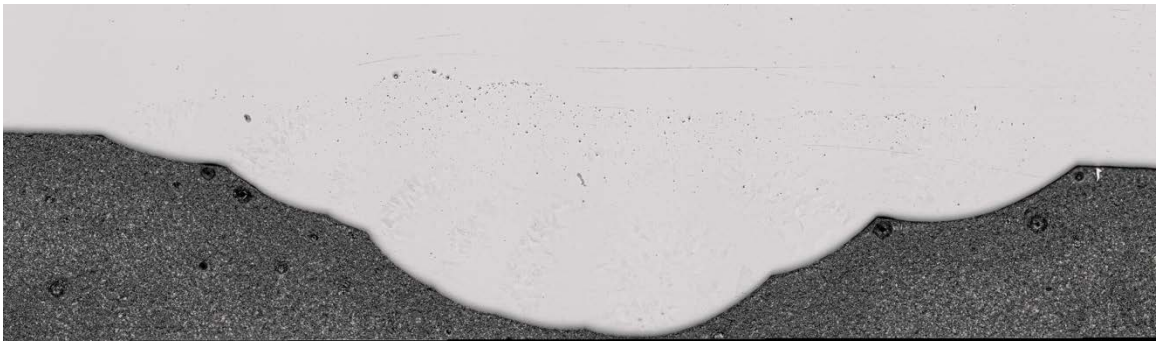

(d) 304D-1-MS4 low speed, ABSI

Figure 17 Cross-section view of laser weld 304D-1 (15.6 ammp He)

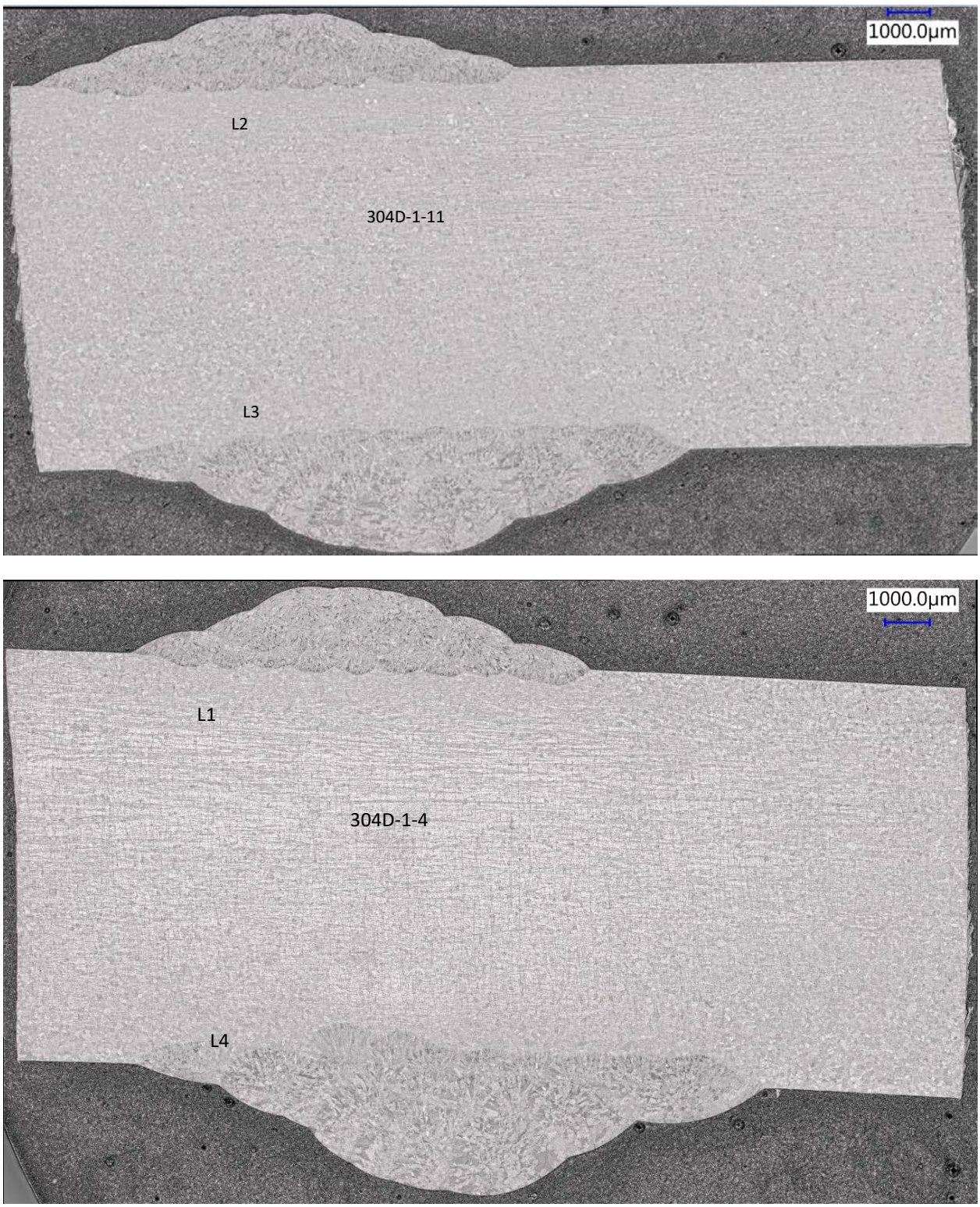

Figure 18 Cross-section view of laser weld 304D-1 (15.6 ammp He)

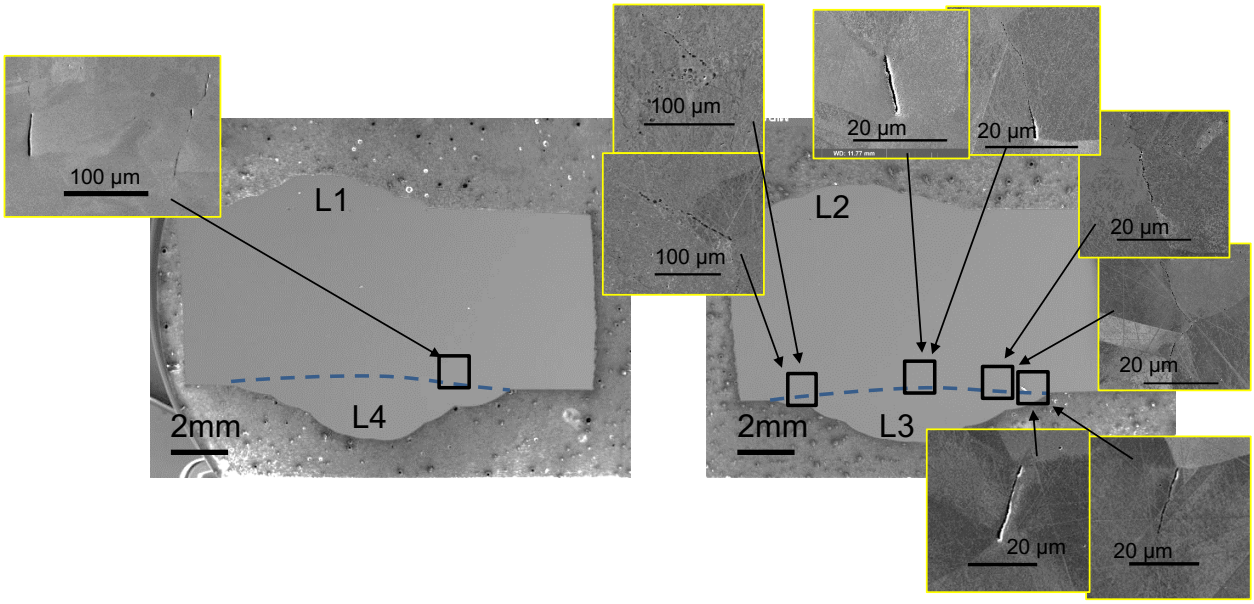

Figure 19 Microcracks under high magnification SEM. Left: Weld 4 (ABSI LW). Right: Weld 3 (LW without ABSI)

5. WELD PROPERTY EVALUATION

As revealed in the detailed characterization of microstructure and microscopic features for 304C-6 FSW with 5.2 appm helium (Milestone Report M2LW-19OR0406014 “Develop Parameters and Characterize the Quality of Friction Stir and Laser Weld-Repaired, Irradiated Structural Materials Representative of Extended Reactor Service Life” (April, 2019)), the microstructure and hardness are highly inhomogeneous in FSW. In this report period, miniature tensile specimens were EDM machined from different regions of 304C-6-15 section (Figure 12) to evaluate the tensile strength of the weld region at room temperature.

Figure 20 shows the locations of the mini-tensile specimens relative to the FSW. Three tensile specimens, all across the entire FSW, are labeled as Long (L), Medium (M), and Short (S) in the figure. Miniature tensile specimens were designed; gauge dimensions were increased as necessary to cover all areas of interest and maximize the irradiated material utilization. Specimen geometry was selected to fit the existing grips (both for ex-situ and in-situ tensile test. Using the existing grips will help to reduce project time and cost. Gauge width (0.8 mm) was kept the same for all cases.

We note that the Long specimen and Short specimen covered the weld region that had micro voids and weld tool debris described earlier. The Medium specimen was taken from the middle section of the weld which was relatively “defect-free” compared to two other regions..

For comparison, three mini-tensile specimens from a FSW made of unirradiated SS304 stainless steel were also tested under the identical condition to compare with the results from the irradiated FSW. The locations of the unirradiated mini-tensile specimens were taken from the same locations in Figure 20.

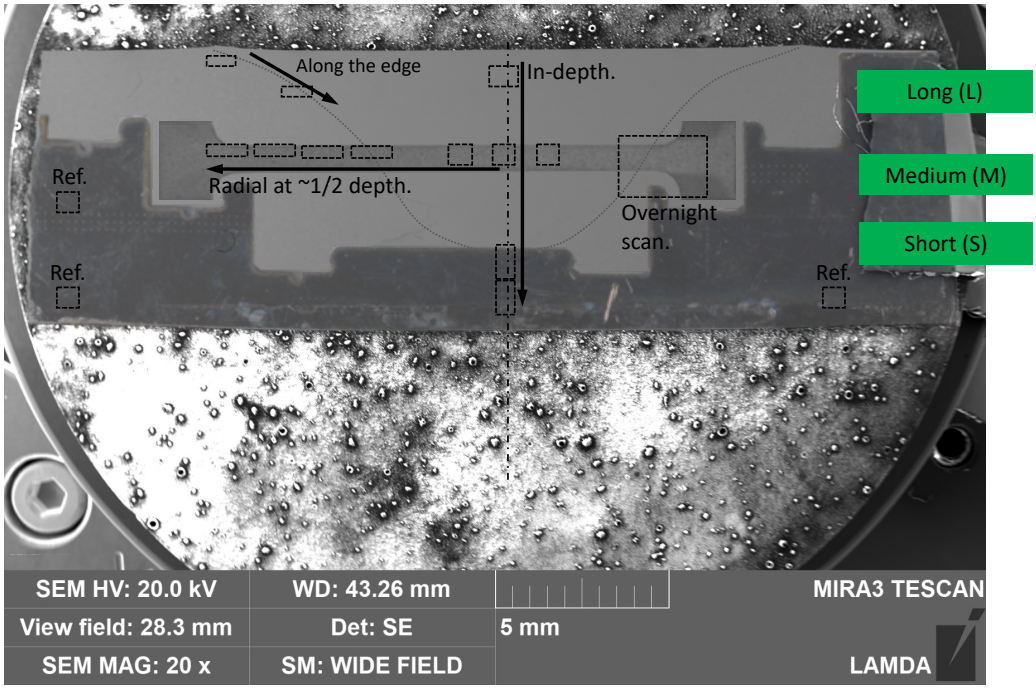

Figure 20 Locations of the mini-tensile specimens relative to the FSW. Three tensile specimens

The mini-tensile specimens were painted with DIC patterns prior tensile test. So the local deformations/failures at different regions of the weld in a tensile specimen can be studied and related to weld microstructures and micro-sized or macro-sized defects (if any). The DIC measurement data are still under study, and expected to be reported in future reporting periods.

The mini-tensile testing results are summarized in Figure 21. The thin lines in the plots are reference from the unirradiated FSW. While the failure of the all three tensile specimens from the irradiated FSW exhibited relatively "ductile" failure, the considerable variations of the ultimate tensile strength from different locations of the FSW suggests potential weld defects (not necessarily helium or irradiation induced brittleness). In particular, the Long specimen only had an ultimate tensile strength of 420MPa, compared to that of 540MPa and 570MPa of Medium and Short specimens, respectively. These considerable variations in strength, in connection to the observed microcracks in the HAZ of FSW, suggests further FSW process refinement would be necessarily.

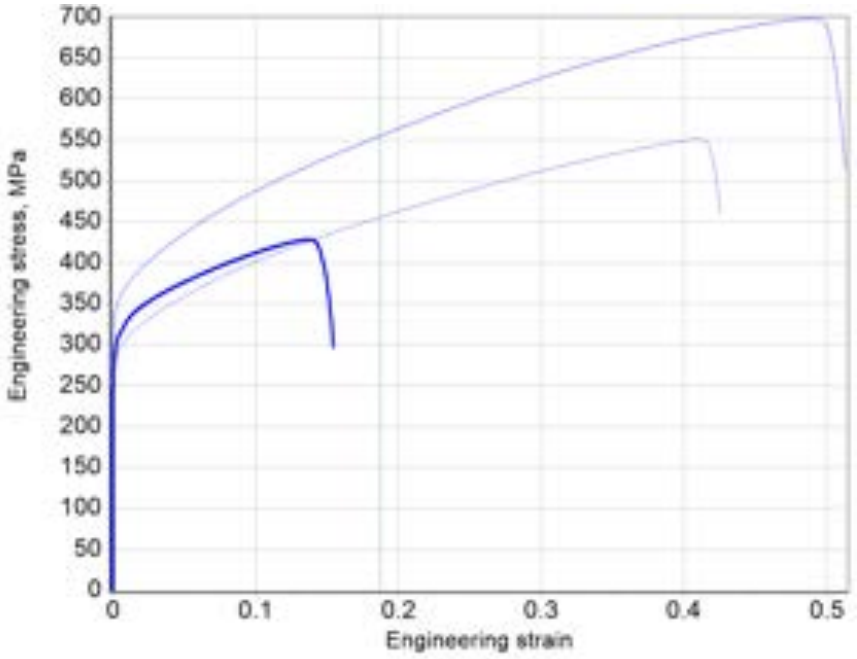

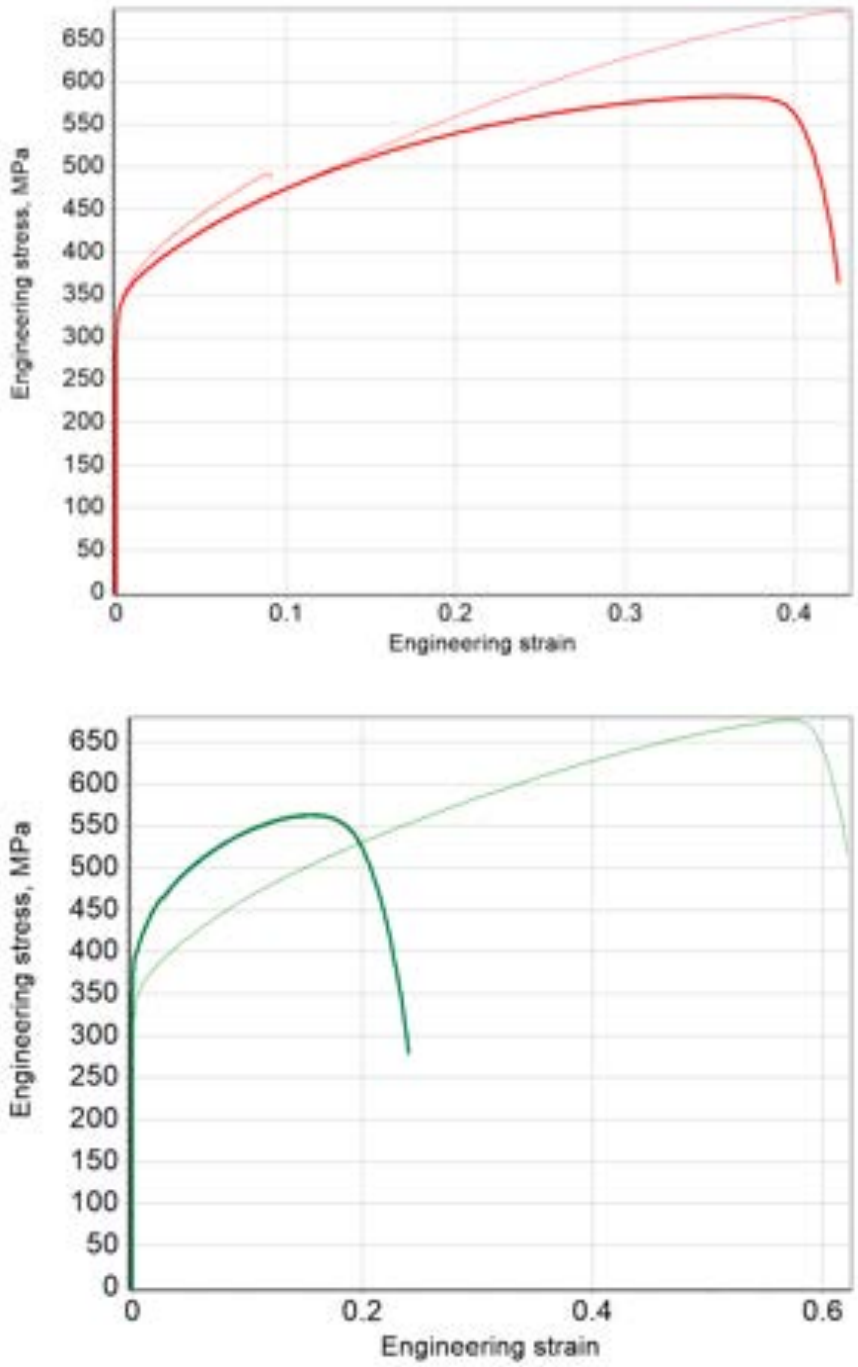

Figure 21 Engineering stress-strain curves from mini-tensile specimens. Top: Long Specimen, Middle: Medium Specimen, Bottom: Short specimen.

6. SUMMARY

This report describes the post-weld study of weld quality and weld properties of irradiated 304 stainless steel made using both Auxiliary Beam Stress Improved Laser Welding (ABSI-LW) and Friction Stir Welding (FSW) processes and conducted in FY 2019. The results demonstrate that both ABSI-LW and FSW processes, developed in this program, mitigated helium-induced cracking during weld repair of helium-containing irradiated SS304 stainless steels. The ABSI-LW method successfully welded SS 304 stainless steel with 15.6 appm He, which is much higher than that has been reported and used by industry. The FSW method successfully welded two different levels of helium (3.4 and 5.2 appm). The findings from this study also suggest pathways to further refine and optimize the two innovative welding processes and possibly the successful welding repair of nuclear reactor internals having helium levels much higher than current weld repair technologies.

This report fulfills the FY2019 milestone M3LW-19OR0406015 “Complete Report on Evaluation of Weld Quality and Weld Properties on Irradiated Stainless Steel Alloys.”

7. BIBLIOGRAPHY

[1] EPRI, "BWRVIP-97, Revision 1: BWR Vessel and Internals Project, Guidelines for Performing Weld Repairs to Irradiated BWR Internals," 2015.

[2] Y. Gong, X. Cao, S. Jin, E. Lu, Y. Hu, T. Zhu, P. Kuang, Q. Xu and B. Wang, "Effect of dislocations on helium retention in deformed pure iron," *Journal of Nuclear Materials,* vol. 482, pp. 92-98, 2016.

[3] L. Ventelon, B. Wirth and C. Domain, "Helium–self-interstitial atom interaction in α-iron," *Journal of Nuclear Materials,* vol. 351, no. 1, pp. 119-132, 2006.

[4] X. Hu, K. Field, S. Taller, Y. Katoh and B. Wirth, "Impact of neutron irradiation on thermal helium desorption from iron," *Journal of Nuclear Materials,* vol. 489, pp. 109-117, 2017.

[5] K. Morishita, R. Sugano, B. Wirth and T. Diaz de la Rubia, "Thermal stability of helium–vacancy clusters in iron," *Nuclear Instruments and Methods in Physics Research Section B: Beam Interactions with Materials and Atoms ,* vol. 202, pp. 76-81, 2003.

[6] C.-C. Fu and F. Willaime, "Interaction between helium and self-defects in α-iron from first principles," *Journal of Nuclear Materials,* Vols. 367-370, no. 244-250, 2007.